

**Analysis of Aircraft Measurements of Atmospheric
Turbulence**

**16 April, 2009
FINAL REPORT AOARD SPC 06-4090**

**Dr. Don Wroblewski
Zentropy Consulting, LLC**

**Prime Contractor
Airborne Research Australia
Dr. Jorg Hacker**

**AOARD Program Manager
Rengasamy Ponnappa**

**AFRL Contact
Dr. Owen Cote**

Report Documentation Page

Form Approved
OMB No. 0704-0188

Public reporting burden for the collection of information is estimated to average 1 hour per response, including the time for reviewing instructions, searching existing data sources, gathering and maintaining the data needed, and completing and reviewing the collection of information. Send comments regarding this burden estimate or any other aspect of this collection of information, including suggestions for reducing this burden, to Washington Headquarters Services, Directorate for Information Operations and Reports, 1215 Jefferson Davis Highway, Suite 1204, Arlington VA 22202-4302. Respondents should be aware that notwithstanding any other provision of law, no person shall be subject to a penalty for failing to comply with a collection of information if it does not display a currently valid OMB control number.

1. REPORT DATE 22 JUL 2009	2. REPORT TYPE FInal	3. DATES COVERED 14-03-2007 to 15-07-2009			
4. TITLE AND SUBTITLE Analyses of Aircraft Measurement of Atmospheric Turbulence		5a. CONTRACT NUMBER FA48690710016			
		5b. GRANT NUMBER			
		5c. PROGRAM ELEMENT NUMBER			
6. AUTHOR(S) Jorg M hacker		5d. PROJECT NUMBER			
		5e. TASK NUMBER			
		5f. WORK UNIT NUMBER			
7. PERFORMING ORGANIZATION NAME(S) AND ADDRESS(ES) ARA-Airborne Research Australia Pty Ltd,PO Box 335,Salisbury South 5106,Australia,AU,5106		8. PERFORMING ORGANIZATION REPORT NUMBER N/A			
9. SPONSORING/MONITORING AGENCY NAME(S) AND ADDRESS(ES) AOARD, UNIT 45002, APO, AP, 96337-5002		10. SPONSOR/MONITOR'S ACRONYM(S) AOARD			
		11. SPONSOR/MONITOR'S REPORT NUMBER(S) AOARD-064090			
12. DISTRIBUTION/AVAILABILITY STATEMENT Approved for public release; distribution unlimited					
13. SUPPLEMENTARY NOTES					
14. ABSTRACT The analysis of high resolution turbulence measurements obtained over 8 years from a unique aircraft platform have shed light on the phenomena of clear air turbulence (CAT) and optical turbulence (OpT) in the Upper Troposphere and Lower Stratosphere (UTLS) and how they may adversely impact systems of interest to the Air Force. Some notable results include 1. Characterization of cliff-ramp patterns and the use of DNS to provide insight into how cliff-ramps can be used to infer characteristics of CAT layers. 2. The first-of-its kind compilation of structure function behavior at sub km-scales from a large data set of UTLS measurements, and in particular the identification of the decoupling of small and large scale behavior. 3. The development of a simple EXCEL-based tool for quickly visualizing Richardson number profiles from radiosonde data, providing a global but coarse view of turbulence potential. 4. Identification of scale-dependent behavior of length scale ratios critical for structure parameter modeling. In spite of this progress, the full potential of this work will be achieved only with continued effort to address critical questions that inevitably arose as part of such an extensive multi-year effort. These include the connection between Richardson number and CT2, the effect of time dependency seen in DNS of stratified turbulence and its affect on the ability to predict both CAT and OpT, and the importance of scale-dependent behavior of the length scale ratios for model development. The author hopes that the results of work reported here will provide motivation for further experimental campaigns and more detailed comparisons between field data and direct numerical simulations in an effort to further our understanding of stratified turbulence and its impact on Aerospace systems.					
15. SUBJECT TERMS Atmospheric Science, Turbulence, Aircraft Control					
16. SECURITY CLASSIFICATION OF:			17. LIMITATION OF ABSTRACT Same as Report (SAR)	18. NUMBER OF PAGES 39	19a. NAME OF RESPONSIBLE PERSON
a. REPORT unclassified	b. ABSTRACT unclassified	c. THIS PAGE unclassified			

Table of Contents

1.0 Introduction	3
2.0 Measurements	4
3.0 Cliff Ramps and Kelvin Helmholtz	5
4.0 Structure Function Analysis.....	8
5.0 RiNLAW	16
6.0 Length Scale Filtering	17
7.0 Concluding Remarks	18
8.0 Acknowledgments	19
9.0 References	20
Tables	25
Figures	28

1. Introduction

Turbulence in the Upper Troposphere and Lower Stratosphere (UTLS) can adversely impact performance of a range of aerospace systems. Optical Turbulence (OpT) from fluctuations in temperature and humidity can affect electromagnetic propagation, disrupting communications, radar, high energy laser systems, and space imaging. Similarly, Clear Air Turbulence (CAT) can lead to aircraft upset, a problem particularly acute for stratospheric vehicles that often must fly within a narrow flight envelope. Thus, reliable prediction is critical for turbulence avoidance and mitigation in these operational situations. Unfortunately, prediction is difficult due to the nature of UTLS turbulence, which is concentrated in very thin layers of hundreds of meters to a few kilometers, a scale smaller than the typical resolution of meso-scale weather forecasting models. As such, prediction and forecasting rely on parameterized models, based on statistical correlations and phenomenological relations between meso-scale parameters and turbulence quantities, to identify regions that have the potential for high levels of clear air or optical turbulence. These approaches are only as good as the fundamental understanding of UTLS turbulence structure that forms the underlying foundation for the models; such insight must be gleaned from experimental data, detailed micro-scale simulations, highly-nested meso-scale model runs, or a combination of all three.

The work presented in this final report addresses a gap in published experimental data for turbulence of scales in the range from approximately 1 meter to 1 kilometer in the upper troposphere and lower stratosphere (7 to 14 km), using high resolution turbulence measurements of temperature, and all three components of velocity, obtained with the EGRETT aircraft as part of a multi-year effort (1998-2006) to study CAT and OpT. The overall objective of the work was to probe the small scale structure of UTLS turbulence, in the hopes of furthering our understanding of atmospheric phenomenon in general and of providing data for building and testing more effective parameterized models for prediction and forecasting.

2. Measurements

Aircraft measurements were acquired with the Grob 520T EGRETT aircraft, the sole twin-seat version of the four GROB 520 aircraft produced, which is operated by Airborne Research of Australia and Flinders University. This high altitude, turbo-prop research aircraft is capable of operation at altitudes up to 15 km at airspeeds of approximately 100 m/s with an endurance of 8 hours. The aircraft can accommodate up to three NOAA/FRD built BAT probes (Crawford and Dobosy, 1992, 1997), one located under each wing, and one located at the top of the tail. The BAT probes consists of a 13-cm diameter hemispherical with nine pressure ports for measurement of all three components of wind velocity and a micro-bead thermister located inside the central dynamic pressure port, for temperature measurement. Beginning in 2002, the NOAA FUST (Fast Ultra-Sensitive Temperature) probe was also mounted externally on the top of the BAT probe body. This bare wire, micro-thermocouple sensor generally featured lower signal-to-noise than the thermister, so when available, its output was used. For three of the campaigns (described below), the right-wing BAT probe was replaced with a standard Rosemont 5-hole probe with a Rosemont PT50 probe for temperature.

For nearly all flights prior to 2006, velocity and temperature data were sampled at 50, 55.6, or 58.8 Hz, providing horizontal spatial resolution of approximately 1.4 to 2 m. For 2006, the sampling rate was 10 Hz and for the November, 2002, it was 25 Hz, reducing spatial resolution to approximately 10 m and 4 m respectively. Frequency response of the velocity measurements was generally near or above the sampling frequency. On the other hand, the BAT thermister probe had an estimated time constant between 0.02 and 0.03 seconds, depending on the flight conditions, leading to thermal lag drop-off near 20-30 meter scales. Both the FUST and the Rosemont temperature sensors had slightly faster response, but still exhibited drop-off in the 10 to 30 meter scale range.

A typical flight featured several level flight segments at altitudes from 7 km up to 14 km, covering wind-relative distances from 45 to 250 km. (Note that all flight distances specified will be in wind relative coordinates, based on the true air speed of the aircraft). During these level segments, natural fluctuations in the aircraft altitude were less than approximately +/- 40 m. As a general rule, the

segments were flown upwind or downwind, with over 75% of the distances flown associated with angles between wind and flight path of less than 30 degrees. Approximately 5% of the flight distance involved significant crosswind component, with angles greater than 70 degrees. Data was also available for climb and descent between level segments for some flights, and these were used to estimate vertical gradients.

The 129 level flight segments selected for analysis are summarized in Table 1. They represent 41 hours of flight time and 12,600 km of wind relative flight distances. Distributions of several flight parameters, weighted based on the length of each segment in wind relative distance, are shown in Figure 1. The mean altitude was 10.4 km and the mean wind speed was 44.5 m/s, both exhibiting Gaussian-like distributions. The wind direction statistics reflect prevailing westerly jet-streams, with a mean direction of 254 and with 84% of the flight distances within +/- 30 degrees of due west. The flight segment lengths exhibit a skewed distribution, with more than 75% of the flight distance flown in segments less than the mean of 123 km. The tropopause was above 13 km for most of the flight days, not untypical for the mid winter in Southern Australia, so that 87% of the flight distances were below the tropopause. The remaining 13% of the flight distances were flown within the tropopause layer.

3. Cliff-ramps and Kelvin Helmholtz

Cliff-ramp patterns (CR) are a common feature of scalar turbulence, characterized by a sharp temperature increase (cliff) followed by a more gradual temperature decrease (ramp). Cliff ramps were identified in temperature measurements of twenty-six of the 129 UTLS CAT layers and data for three of these were analyzed in detail, Wroblewski et. al, 2007. The results supported the idea that the CR patterns were signatures of Kelvin Helmholtz (KH) billows, with the ramps associated with the well mixed billows and the cliffs marking the highly-stretched braids.

Direct Numerical Simulations (DNS) of stratified turbulence by Joe Werne from CORA/NWRA, work that was also funded by AFRL, have revealed new insights into the Kelvin Helmholtz (KH) phenomenon and its role in the development of CAT layers in the atmosphere (Werne et al., 2005, 2008), including the presence of cliff ramps. In addition, his work has shown that the nature of the KH

development is strongly affected by the initial Richardson number of the layer; $Ri = N^2/S^2$, where S is the

shear rate, $S = \frac{\partial u_L}{\partial z} + \frac{\partial u_N}{\partial z}$, and N is the buoyancy frequency, $N = \left(\frac{g}{\Theta} \frac{\partial \Theta}{\partial z} \right)^{1/2}$, where Θ is the mean

potential temperature.

Data for ten aircraft measurement CR cases were compared qualitatively and quantitatively to Werne's DNS, in an effort to predict the initial Ri number of the layer, an idea that the authors attribute to Joe Werne. This work is summarized in the following sections.

3.1 Qualitative comparisons of Aircraft Data and DNS

Transects through the DNS revealed distinct patterns in the temperature signal—cliff-ramps, step-cliffs and buttes, all characterized by steep cliffs. Based on the strength and character of these patterns, qualitative comparisons of the ten aircraft flight with the DNS transects were used to estimate the vertical location (Centerline or Off-centerline), initial Ri (Med—closer to 0.15, High—closer to 0.2, or Indeterminate) and cliff-ramp development stage (Early, Mid, or Late). The following criteria were used for making these estimates:

- Cliff-ramps only with sharp edges: Centerline, High Ri , Late
- Cliff-ramps and Step-cliffs with velocity cliffs: Centerline, High Ri , Mid
- Cliff-ramps and Step-cliffs without velocity cliffs: Centerline, Mid Ri , Mid
- Any cliff in the process of breaking down: Late
- Buttes or rounded edges to Cliff-ramps: Off-centerline, indeterminate Ri .

As an example, Figures 2 and 3 shows comparisons for two flights with corresponding DNS transects. The 11.4 km level on 000606 (Fig. 2) features classic cliff-ramp patterns with sharp transitions, suggesting a near center-line location and the lack of any step-cliffs is indicative of a time towards the end of the CR phase of the billow development. Similarly, the 14.3 km level on 020830 (Fig. 3) exhibits a mixture of “buttes” with rounded edges and cliff-ramps suggesting an off centerline location. Table 2 shows a summary of the qualitative estimates.

3.2 Quantitative comparisons of Aircraft Data and DNS

More quantitative comparisons of aircraft data and DNS were accomplished with a method based on the variation of non-dimensional temperatures change across the cliff, $\Delta\theta/\beta\lambda$ (where β is the mean potential temperature gradient and λ is the wavelength of the cliff ramps) with the initial Ri of the layer. Figure 4 shows this variation for DNS transects at $z/H=0$ and $z/H=0.125$; DNS data in the plots are for $Ri=0.15$ and 0.2 for two different phases of the CR development: (1) when cliff-ramps first appear and (2) when they are no longer seen. The dashed lines are a quadratic curve fit to the points, assuming a zero value at $Ri=0.25$. The vertical lines represent estimates for the various aircraft measurement case, with the range bounded by the two estimates based on the DNS curves for the initial and final phase of CR development-- Ri_1 to Ri_2 . The most striking result is that all but one of the flights features Ri values ≥ 0.15 , the range where CRs were most prominent in the DNS. Even for the one exception, 031122, the upper end of the range of values is close to 0.15. This result is significant, because this approach does not constrain the aircraft values of $\Delta\theta/\beta\lambda$ to values within those predicted by the DNS, providing a level of validation for this approach. Also note that for five of the six centerline cases, the range of initial Ri is close to that estimated from the qualitative estimates.

Figures 5 shows the variation with Ri of the initial and maximum billow heights, normalized on billow wavelength, obtained from the DNS. The corresponding curve fits to this data were used along with the calculated Ri values and the CR wavelengths identified in the temperature signal to determine the initial and final layer heights for the aircraft flights. (Note that the final layer height here refers to the height when the cliff-ramps are observed). As seen in Table 3, two values of height are reported for each flight—e.g., H_1 and H_2 for the final layer height—corresponding to the values calculated with Ri_1 and Ri_2 . The final layer heights ranged from 130 m for the 031122 flight up to 2.0 km for the 990806 case, the only case with a height over 1 km. This is consistent with observations that turbulent layers in the upper troposphere and lower stratosphere occur in thin layers less than 1 km.

The definition of the Ri used for the DNS provides a means for estimating a scaling velocity, U_0 , and the initial shear rate, S_0 , of the layer for the aircraft flights:

$$U_0 = \sqrt{\frac{g \beta h^2}{\theta Ri}} \quad S_0 = \frac{U_0}{h} \quad (1)$$

As in the case of the layer heights, two values are shown in Table 3 for each of these quantities: $U_{0,1}$ and $S_{0,1}$ calculated using Ri_1 and h_1 , and $U_{0,2}$ and $S_{0,2}$ calculated using Ri_2 and h_2 . The scaling velocities range from 1.4 m/s for the 031122 layer to 18.3 m/s for the 990806 layer, while the shear values span a much smaller range, from 0.024 s^{-1} for 990806 to 0.054 s^{-1} for the 990213 layer. The calculated shear rates for six of the ten aircraft layers fall within $\pm 10\%$ of values measured from the velocity data during proximal climb and descent segments, and two others are within $\pm 25\%$.

From the DNS, the temperature signal exhibited cliff ramps for 5.0 shear times ($5U_0/h$) at $Ri=0.15$ and 11.5 shear times for $Ri=0.20$. These values were extrapolated using a linear trend to estimate the duration of cliff-ramps for each of the aircraft flights, with resulting values ranging from 1 to 8 minutes (Table 3). If the observed turbulence layers and cliff-ramps are signatures of developing Kelvin-Helmholtz billows, the time window over which the cliff-ramps can be observed is quite small. This combined with the observation from DNS that the cliff-ramps are only seen within a narrow region near the center of the billow indicates that the observation of cliff-ramps in aircraft measurements is a fortuitous event, and may suggest why only 26 out of 129 CAT levels revealed such patterns.

4. Structure Function Analysis

Structure functions and structure constants were calculated from the time series of velocity and temperature

$$D_{LL}(r) = \langle [u_L(t + r/V_{TAS}) - u_L(t)]^2 \rangle \quad (2)$$

$$C_L^2 = D_{LL}(r) / r^{2/3} \quad (3)$$

where u_L is the component of the wind along the direction of the separation distance vector, \vec{r} -- the direction of the flight path in this case. V_{TAS} is the true airspeed of the aircraft, and the bracket symbols, $\langle \rangle$, denote ensemble averaging. Similar equations were used for D_{NN} the structure function for the component of velocity normal to \vec{r} u_N ; D_{WW} the structure function for the vertical velocity, w ; and D_{TT} the structure function for the temperature, T . Turbulent kinetic energy dissipation was estimated using an isotropic relation

$$\varepsilon = (C_L^2 / 2)^{3/2} \quad (4)$$

Average structure functions were found for each flight segment for 51 values of r , evenly spaced in logarithmic terms, from 2 m to 31 km, resulting in approximately 12 data points per decade. The actual separation distances, r_A , for each segment varied due to differences in true air speed and sampling rates, so values at the 51 specified distances were found by interpolation of the two surrounding values of r_A using a power law fit, r^n . Values for n were also found for ranges of r that displayed linear behavior on log-log plots, by curve fitting a power law to the linear regions. The average structure functions for the individual flight segment were combined to determine composite structure functions for all 129 levels, using averages weighted on the number of data points for each flight-segment-average.

Short-time structure parameters were calculated by dividing each segment into lengths of 1, 5, 10 and 45 km, the latter representing the minimum segment length. For each segment, values of C_L^2 , C_N^2 and C_W^2 were calculated using Eqn. 3 with a separation distance of 30 m and values of C_T^2 were found at a distance of 90 m, and averaged over the 4 different lengths.

Details of the analysis can be found in Wroblewski et al., 2009. Only a summary of key results will be presented here.

4.1 Structure functions for individual segments

Figure 6 includes structure functions for selected individual levels, chosen to span the entire range of turbulence strength at smaller scales and to show the diversity of behavior. The two distinct features of these curves are the plateau levels, most evident in the D_{WW} curves, and the lack of correlation

between the small and large scales. Note that structure functions are similar, though not identical, to cumulative spectra, and thus they can be interpreted in a similar manner, so a plateau region indicates a range of scales with little or no energy. The intermediate plateau in curves 3 and 4 in the D_{LL} plot and curve 4 in the D_{WW} plot indicate a distinct separation of small and large scale. The extended flat plateau for curves 1, 2 and 3 for D_{WW} indicate some limiting scale for the vertical fluctuations that is not seen in the horizontal fluctuations, presumably the thickness of the CAT layer itself. The extended plateau shapes seen in the D_{WW} curves can be recreated by low pass filtering D_{LL} curves that extend to large scales, further suggesting a limiting vertical scale.

In Fig. 7 the solid lines show the distributions of the 3D scaling range structure function exponents (e.g., n_L , where $D_{LL} \propto r^{n_L}$). The n_L distribution is fairly narrow with a peak essentially at $2/3$ with 93 % of the cases displaying an exponent between 0.3 and 0.78. The distributions for n_N and n_T are similar to those of n_L , with peaks between 0.6 and 0.7, but with shapes skewed towards higher values. For n_w the distribution is much broader with more values below 0.3 (15%). The mean values of the exponents are close to the peak values: 0.61 for n_L , 0.69 for n_N and n_T and 0.62 for n_w . Although 79 of the 129 cases (61%) indicate an inertial-range value of n_L close to $2/3$ (0.55 to 0.8), only 21 of those have values of n_N , n_w , and n_T in that range as well. The dashed lines show distributions for scaling exponents at the 10 km scale. These distributions for n_L , n_N , and n_T are much broader than the corresponding ones in the 3D scaling sub-range, with higher average values—0.85 for n_L and n_N , and 0.79 for n_T . In contrast, the n_w distribution has a sharp peak at 0, reflecting the plateau-like behaviors seen in Fig. 6.

Fig. 8a shows the distributions of structure constants C_L^2 and C_T^2 , obtained from the force fit of D_{LL} and D_{TT} to an $r^{2/3}$ power law in the identified 3D scaling range. These are well matched the lognormal distributions (lines in the figure) predicted by Kolmogorov (1959) for dissipation and as shown by FS05. The upper scale in Fig.8a indicates the dissipation values corresponding to the C_L^2 distribution based on Eqn. 4. The means and standard deviations of the log distributions are as follows:

$$\langle \log_{10} C_L^2 \rangle = -2.87; \quad \sigma_{\log_{10} C_L^2} = 0.719; \quad \langle C_L^2 \rangle = 5.51 \cdot 10^{-3} \text{ m}^{4/3} \text{ s}^2 \quad (5)$$

$$\langle \log_{10} \varepsilon \rangle = -4.77; \quad \sigma_{\log_{10} \varepsilon} = 1.08; \quad \langle \varepsilon \rangle = 3.57 \cdot 10^{-4} \text{ m}^2 \text{ s}^{-3} \quad (6)$$

$$\langle \log_{10} C_T^2 \rangle = -4.29; \quad \sigma_{\log_{10} C_T^2} = 0.749; \quad \langle C_T^2 \rangle = 2.77 \cdot 10^{-4} \text{ K}^2 \text{ m}^{-2/3} \quad (7)$$

The distributions of the structure parameters for the normal and vertical velocities are reported in Figure 8b in the form of ratios with C_L^2 ; this ratio should be 4/3 for an isotropic, homogeneous inertial range. The peak of the log distribution for C_N^2/C_L^2 corresponds to a value of 1.2, close to the isotropic value of 4/3. However, only 44 of the 129 levels (about 1/3) display a value within $\pm 20\%$ of the isotropic value. The log distribution for C_W^2/C_L^2 exhibits significantly different behavior, centered on a peak corresponding to 0.40, and with only 3 of the 129 levels showing a value within $\pm 20\%$ of the isotropic value. This is consistent with the idea that the stratification is limiting both the scale as well as the intensity of the vertical fluctuations.

4.2 Composite structure functions and parameters

Composite structure functions for velocity and temperature as a function of separation distance are shown in Figure 9. The solid curves represent values for the entire ensemble of 129 levels, while the other three curves are for sub-ensembles filtered based on the C_L^2 or C_T^2 values in the 3D scale range-- strong turbulence ensemble, containing all levels with values of $\log_{10}(C_L^2)$ or $\log_{10}(C_T^2)$ greater than $1/2$ standard deviation above the mean values (see Eqns. 6 and 7); moderate turbulence ensemble, made up of levels with values of $\log_{10}(C_L^2)$ or $\log_{10}(C_T^2)$ within $-1/2$ and $1/2$ standard of the mean, and weak turbulence ensemble, consisting of levels with values of $\log_{10}(C_L^2)$ or $\log_{10}(C_T^2)$ less than $-1/2$ standard deviation below the mean. Scaling range exponents and structure parameters are shown for these ensembles in Table 4.

The 3D scaling range for the velocity extends from 2 to about 100 meters, with exponents close to the theoretical value of 2/3 for D_{LL} and D_{NN} , but larger for D_{WW} . The exponents are similar for the two stronger sub-ensembles, but are much smaller for the weak turbulence case. The scaling range for temperature is between 100 and 1000 meters, with an exponent of 0.7 for all sub-ensembles. Consistent with statistics of individual flight levels, the normal and vertical velocity structure parameters reflect non-

isotropic behavior, with C_N^2/C_L^2 between 0.8 and 1.0 for the various sub-ensembles and between 0.6 and 0.64 for C_W^2/C_L^2 . For both D_{LL} and D_{TT} , the behavior at large scales is nearly the same for all ensembles, more so for D_{TT} , consistent with the notion of decoupling of the 3-D and quasi 3-D sub-ranges. This is also true to a lesser degree for D_{WW} , with the weaker turbulence cases displaying curves without plateau levels

Based on the behavior of the composite structure functions, as well as the individual level curves shown in Fig. 6, the range of scales from 2 to 30,000 m may be classified into 3 sub-ranges:

- *3D “inertial” sub-range*, represented by scales less than approximately 100 meters, within which the horizontal velocity and temperature structure functions are close to $r^{2/3}$ behavior and D_{WW} values are on the same order as the horizontal values.
- *Quasi 2D sub-range* from about 5 km to 30 km, where D_{WW} values fall to less than 10% of the horizontal structure functions. Note that in Lindborg (1999), this range is referred to as 3 dimensional, but that designation is based on indirect evidence rather than actual velocity measurements. The upper bound of this range is approximately the thickness of atmosphere, which should be the relevant lower bound for pure 2-dimensional turbulence.
- *Transition sub-range* from 100 meter to 2 km, within which the horizontal velocity and temperature structure functions change slope to adjust to the difference in values in the adjacent $r^{2/3}$ regions, and D_{WW} levels off to reflect the transition from 3-D to quasi 2-D behavior

4.3 Vertical length scales from D_{WW}

The plateau levels seen in 69 of the 129 D_{WW} curves may be indicative of a limiting vertical scale for vertical velocity, which can be interpreted as the vertical height of the turbulence layer. In these cases, hereafter referred to as the layer-height cases, the D_{WW} curves were used for estimating the layer height, Z . The procedure involved low pass filtering the u_L time series (with a 4th order Butterworth filter), resulting in a D_{LL} plot that exhibited a plateau level preceded by a hump similar to those seen in D_{WW} curve 3 of Fig 6. The layer height was assumed to be equal to the filter cutoff wavelength that produced a hump in the filtered D_{LL} curve that best matched the location of the hump in the unfiltered

D_{ww} . The resulting estimates of Z ranged from 80 meters to 2.7 km, as shown in Figure 10, with a distribution that features a peak near 300 m and a smaller peak near 1 km.

Although it remains to be seen whether this method provides useful estimates for the layer height, the results seem reasonable in two respects. First, the overall range of values is consistent with the notion that CAT layers vary in height from hundreds of meters up to a few km. Second, for several of the flights, the climb segments near the level flight altitudes extended far enough above and below the turbulent layer to provide some indication of its thickness. As seen in Fig. 10, the estimates from D_{ww} agree well with those from the climb data.

The layer height cases generally feature stronger turbulence than those without a plateau or hump in D_{ww} ; they include the 20 levels with the strongest small scale turbulence, based on C_L^2 , as well as 31 of the top 33, and 57 of the top 80. The average C_L^2 for these 59 cases is 9 times larger than the average of the 60 non-plateau cases and the average C_T^2 is 16 times larger. This is further illustrated in Figure 11, with composite structure functions for three sub-ensembles of levels: (1) Layer height cases with $Z > 700$ m (20 levels); (2) layer height cases with $Z < 700$ m (49 levels); and all other levels (60 levels). The D_{LL} composite curves all display a sub-range with $r^{2/3}$ scaling behavior, but the two layer-height ensembles also feature a region with slope (power law exponent) near 0.5 in a region corresponding to the location of the plateau in D_{ww} . At scales near 10 km, the D_{LL} curves all converge, again illustrating the lack of correlation between small scale and large scale behavior.

The results of the layer height analysis raise two questions: (1) why do only some levels display such a plateau? And (2) why do these cases feature the strongest small scale turbulence? To answer question (2), consider how the stratified turbulence layer develops. The roll up and overturning of the KH billows is controlled by stratification, a process that limits the largest vertical velocity scale. During billow breakdown and transition, the turbulence and its length scales are largest, and even after the billows are no longer obvious and the flow is three-dimensional, their footprints are still seen in the large scale structures. So, the presence of the plateau is a marker of this highly turbulent transition phase, when the vertical motions on the scale of the billow height are constrained. In support of this idea, 26 of the

layer-height cases also feature cliff-ramps patterns in the temperature signal. Wroblewski et al. (2007) and Whiteway et al (2003) showed that these are signatures of KH billows, with the rapid change in temperature of the cliff associated with the aircraft passing through the steep gradients of the braid separating adjacent billows. There is also evidence that these cliff-ramps are seen primarily during the transition to turbulence phase (Wroblewski et al, 2007).

4.4 Short time structure parameters

Short time structure functions provide statistics on the horizontal homogeneity in and around CAT layers, and are useful for two important reasons. First, electromagnetic waves that are pulsed for short durations (~ 10 seconds) only sample a small portion of a CAT layer, and experience optical turbulence that is substantially different than the overall mean values shown in Fig. 8a. Second, decision aids and propagation models that utilize thermosonde measurements often adopt the “onion-skin” assumption of horizontal homogeneity. But, radiosonde balloons move with the mean wind, so they sample the same air parcel as they ascend through the layer, and spend only a few minutes in many CAT layers; thus, they likely do not experience the full extent of the horizontal variations.

Variations of short-time C_T^2 and dissipation, ε , are shown in Fig. 12 for 1 km and 10 km averaging windows; C_T^2 is shown for the case with the largest variation in C_T^2 (3 orders of magnitude) and likewise for dissipation (6 orders of magnitude). Although the 10 km averaging window filters out the smaller scale fluctuations seen with the 1 km window, the overall peak-to-peak variations are nearly the same. This effect can be seen in Fig. 13, which shows that the log distributions of short-time ε and C_T^2 are nearly the same for all four of the averaging windows (1, 5, 10 and 45 km), and in Fig. 14, which shows the mean and standard deviation of the log normal distributions as a function of averaging window size.

The mean and standard deviations for the smallest three separation distances were curve fit using the fitting equations from Freilich and Sharman, 2005 (FS05):

$$\langle \log \varepsilon \rangle = 0.151 \log L - 5.64 \quad \sigma_{\log \varepsilon} = 1.606 L^{-0.026} \quad (8)$$

$$\langle \log C_T^2 \rangle = 0.128 \log L - 4.90 \quad \sigma_{\log C_T^2} = 1.032 L^{-0.027} \quad (9)$$

The curves fits based on these equations are shown in Fig. 14 as dotted lines, and those from FS05 based on meso-scale model runs are shown as well. The trends shown by these curve fits are qualitatively similar to those from FS05, but the slopes are significantly smaller, reflecting the insensitivity to averaging window. The quantitative disagreement with FS05 results may be due to the difference in the averaging schemes-- the FS05 results are based on spatial averaging rather than time averaging. However, as mentioned above, the raw data seen in Fig. 12 indicate that the structures responsible for the horizontal variations may be larger than 45 km, so the large variations would not be expected at smaller averaging windows. This change in behavior at larger scales is suggested in Fig. 14 by the results for the 45 km lengths and for the average of the level averages (distinguished by the box around the data points), which exhibit a trend that is deviating from the behavior at smaller averaging lengths towards the behavior seen in the FS05 results.

Suppose that a thermosonde profile indicates an elevated C_T^2 value at some altitude, suggestive of a CAT layer. This represents a single realization of the turbulence in the layer; but, it would be useful for decision aids to know the probability of finding stronger turbulence in the same layer. This can be accomplished using the short-time C_T^2 data and conditional probabilities. In particular, $P[(C_T^2)_1 | (C_T^2)_0]$ represents the conditional probability of finding a value of $(C_T^2)_1$ in a layer given that the layer has a value identified by the thermosonde of $(C_T^2)_0$.

Conditional PDFs were found from the 1 km window C_T^2 data and are plotted in Fig. 15 for 6 ranges of values of $\log (C_T^2)_0$: -6.55 ± 0.15 , -5.65 ± 0.15 , -4.75 ± 0.15 , -3.85 ± 0.15 , -2.95 ± 0.15 , and -2.05 ± 0.15 . The conditional PDFs are based on conditional ensembles of all layers with at least one realization of the corresponding value of $(C_T^2)_0$, and can be interpreted in the following manner: given at least one realization of $(C_T^2)_0$ in a layer, what's the probability distribution of a randomly chosen realization. As expected, the distributions shift to higher values for higher values of $(C_T^2)_0$.

The conditional PDFs were used to generate the conditional probability of finding a value of (C_T^2) greater than some threshold given a single realization value of $(C_T^2)_0$. Two different results are shown in Fig 16 for thresholds of 10^{-4} , 10^{-3} and 10^{-2} for C_T^2 : the top plot shows the probability of a random realization exceeding the threshold; while the bottom plot shows the probability that the layer contains at least one realization greater than the threshold. For example, if a thermosonde indicates a measured C_T^2 value of 10^{-4} (x axis on plots in Fig. 16), then there is a 0.6 % probability that a random realization will be greater than 10^{-2} , but a 9% probability that at least one realization will be greater than 10^{-2} (values circled in Fig. 16).

5. RiNLAW: Richardson Number Layer Analysis Worksheet

RiNLAW is an EXCEL-based tool for quickly analyzing and visualizing Richardson number profiles, using on-line Radisonde data as input. Developed in August 2006, as a planning tool for aircraft measurement campaigns, it has been constantly modified and upgraded to address needs of the AFRL sponsor. In addition to planning flights for the summer 2009 measurement campaign, this tool is being used by AFRL for analyzing unique and persistent Ri layer trends at various sites with the intent of identifying possible adverse impacts on space-to-ground propagation.

The first implementation of RiNLAW was on August 9, 2006 (060809) as a flight planning tool. As seen in Figure 17, the 00Z sounding in Adelaide indicated only a single shear layer (Ri less than the critical value of 0.25) at 8.26 km of approximately 25 m thickness, despite a very strong jet (175 kt peak wind). The EGRETT pilot was briefed on this result, and the flight plan adjusted accordingly. The forecast proved to be accurate, with actual measurements showing turbulent activity between 8,260 km and 8,607 km, almost exactly the same location as the shear layers seen in the radiosonde. It should be noted that analysis of radiosonde data did not always lead to such successful outcomes, due to several factors: the jet may not have been directly over Adelaide or other nearby sounding sights; conditions may not have persisted long enough for the aircraft flight to capture what was seen in radisondes that were

many hours old; and the Ri criteria by itself may not have been sufficient to identify possible layers. Still, the success on 060809 demonstrated the utility of RiNLAW as a component of flight planning.

For campaigns prior to 2006, RiNLAW was used for analyzing conditions for flights that exhibited significant turbulence activity. Table 5 is a summary of the comparisons for 8 cliff-ramp cases. Most of the cases represent mild turbulence, with Eddy Dissipation rates ($EDR=\varepsilon^{1/3}$) in the 0.1 to 0.3 range, with one case of moderate turbulence (EDR in the 0.3 to 0.5 range) and one case of extreme turbulence (EDR greater than 0.5). Given the spatial and temporal separations of the soundings and aircraft flights, the comparisons are quite favorable, with RiNLAW identifying shear layers with Ri less than or close to 0.25 within several hundred meters of measured CAT layers.

Figures 18 through 20 display results several sites that exhibit unique Ri profiles. For the Perth, Australia case (Fig. 18), the majority of the low Ri layers are in the 15 to 26 km range, well above the relatively strong jet. These layers correspond to oscillations in the meridional velocity indicative of wave activity. This effect is seen in its extreme in the Goose Bay profiles in Fig. 19. The Goose Bay case in Fig. 20 reveals several narrow jets at different altitudes which correspond with very low Ri numbers; this behavior seems common at this location. These profiles provide a glimpse of how RiNLAW, coupled with radiosondes available on-line, can provide a global but coarse view of turbulence potential anywhere in the world where a radiosonde station is located.

6. Length Scales for Structure Parameter Modeling

Forecasting of OpT relies on accurate models for C_T^2 in stably stratified conditions. Such models are difficult to formulate due in part to the multitude of length scales that govern turbulence production and decay. Models that are based on fundamental turbulent transport equations have revealed two critical length scale ratios: (Cote, Wroblewski and Hacker, 2009).-- L_{DW}/L_E and L_E/L_B , where L_E is the Ellison scale, L_{DW} is a dissipation length scale, and L_B is a buoyancy length scale:

$$L_E = \frac{\sigma_\theta}{\beta} \quad L_{DW} = \frac{\sigma_w^3}{\varepsilon} \quad L_B = \frac{\sigma_w}{N} \quad (10)$$

In Eqn. 10, σ_θ and σ_w are rms of the potential temperature and vertical velocity, β is the vertical gradient, of the mean potential temperature, $\beta = \frac{\partial \Theta}{\partial z}$.

The ratio L_{DW}/L_E appears in a modified version of the Tatarskii model based on the budget equation for the temperature variance (Cote, Wroblewski and Hacker, 2009); the ratio modifies the outer scale term, the critical parameter needed for model closure.

The ratio L_E/L_B arises in the second order turbulent budget equation for the vertical heat flux, and is equivalent to the ratio of the buoyancy loss term to the dominant production. Although this ratio should be less than 1, it was found to be greater than 1 for several of the strong cliff-ramp cases described in Section 3. From Equation 10, it can be seen that L_E/L_B is proportional to σ_θ/σ_w . These rms values are dominated by the large scale behavior. However, the structure function analysis in Section 4 indicated that D_{WW} is limited at large scales while D_{TT} was not. This, coupled with the fact that large scale behavior is decoupled from the small scale behavior, suggests that calculated L_E/L_B ratios are not reflective of the physics of the small scale behavior. To address this, the ratio was recalculated using “filtered” temperature and velocity data, and example of which is shown in Fig. 21. The filtering was accomplished using cumulative spectra, so a point on the plot represents the ratio found when all scales above the value r (x axis) are filtered out. As seen in the figure, L_E/L_B decreases as more of the large scales are removed, and approaches 1 near the inertial subrange. A similar trend is seen for L_{DW}/L_E .

This analysis was applied to all 129 CAT layers. The distributions of the unfiltered values of L_E/L_B and the values at $r=100$ m are shown in Fig. 22, which clearly show how filtering reduces the values. Note that at $r=100$ m, almost a third of the levels have ratios that are lower than the unfiltered values, but are still greater than 1.

7. Concluding Remarks

The analysis of high resolution turbulence measurements obtained over 8 years from a unique aircraft platform have shed light on the phenomena of clear air turbulence (CAT) and optical turbulence

(OpT) in the Upper Troposphere and Lower Stratosphere (UTLS) and how they may adversely impact systems of interest to the Air Force. Some notable results include:

- Characterization of cliff-ramp patterns and the use of DNS to provide insight into how cliff-ramps can be used to infer characteristics of CAT layers.
- The first-of-its kind compilation of structure function behavior at sub km-scales from a large data set of UTLS measurements, and in particular the identification of the decoupling of small and large scale behavior.
- The development of a simple EXCEL-based tool for quickly visualizing Richardson number profiles from radiosonde data, providing a global but coarse view of turbulence potential.
- Identification of scale-dependent behavior of length scale ratios critical for structure parameter modeling.

In spite of this progress, the full potential of this work will be achieved only with continued effort to address critical questions that inevitably arose as part of such an extensive multi-year effort. These include the connection between Richardson number and C_T^2 , the effect of time dependency seen in DNS of stratified turbulence and its affect on the ability to predict both CAT and OpT, and the importance of scale-dependent behavior of the length scale ratios for model development. The author hopes that the results of work reported here will provide motivation for further experimental campaigns and more detailed comparisons between field data and direct numerical simulations in an effort to further our understanding of stratified turbulence and its impact on Aerospace systems.

8. Acknowledgements

The continued support of Dr. Arje Nachman of AFOSR for this effort is acknowledged. Special acknowledgement goes to the late Timothy Crawford of NOAA who designed and built the turbulence probes and who championed the use of small aircraft for studying big turbulence issues. The authors thank Joe Werne, Colorado Research Associates, Northwest Research Associates for kindly providing his

unpublished DNS results for comparison with field data, and for his input and discussions regarding Kelvin Helmholtz layer development.

9. References

Antonia, R. A., Smalley R. J., 2001, Scaling range exponents from X-wire measurements in the atmospheric surface layer, *Bound. Layer Meteorol.* **100**, pp. 439–457.

Billant, P., and J.-M. Chomaz, 2000, Experimental evidence for a new instability of a vertical columnar vortex pair in a strongly stratified fluid. *J. Fluid Mech.*, **418**, 167–188.

Bolgiano., R., 1959: Turbulent spectra in a stably stratified atmosphere. *J. Geophys. Res.*, **64**, No. 12, 2226-2229.

Chan, K. R., Dean-Day, J. Bowen, S. W., Bui, T. P., 1998, Turbulence Measurements by the DC-8 Meteorological Measurement System, *Geophysical Research Letters*, **25** (9), pp. 1355-1358.

Cho, J. Y. N., Lindborg, E., 2001, Horizontal Velocity Structure Functions in the Upper Troposphere and Lower Stratosphere 1. Observation. *J. Geophys. Res.* **106**, (10), pp. 10,223–10,232.

Cote, O., Wroblewski, D., Hacker, J., “Refractive Turbulence, Transient Electronic Disconnectivity, and Propagation Situational Awareness (PSA) ,” 47th AIAA Aerospace Sciences Meeting, Orlando, 1/2009.

Crawford, T. L. and R. J. Dobosy, 1992: A sensitive fast-response probe to measure turbulence and heat flux from any airplane. *Bound.-Layer Meteor.*, **59**, 257-278.

Crawford, T. L. and R. J. Dobosy, 1997: Pieces to a puzzle: Air-surface exchange and climate. *GPS World*, **8** (11), 32 – 39.

DaSilva, I. P.D., Fernando, J.S., Eaton, F., Hevert, D., 1996, Evolution of Kelvin-Helmholtz billows in nature and laboratory, *Earth and Planetary Science Letters*, **143** (2), pp. 17-23 I

Duck and Whiteway, 2005, Spectrum of Gravity Waves and Turbulence in the Tropopause, *Geophys. Res. Lett.*, 32, L07801, doi:10.1029/2004GL021189,.

Frehlich, R. and Sharman, R., 2005, Estimates of Turbulence from Numerical Weather Prediction Model Output with Applications to Turbulence Diagnosis and Data Assimilation, *Mon. Wea. Rev.*, **132**, pp. 2308-2324.

Gargett, A. E., 1998, The Scaling of Turbulence in the Presence of Stable Stratification, *J. Geophys. Res.*, **93**(C5), pp. 5021-5036.

Garman, K. E, Hill, K.A., Wyss, P., Carlsen, M., Zimmerman, J. R., Stirm, B. H., Carney, T. Q., Santini, R., Shepson, P.B., 2006, An Airborne and Wind Tunnel Evaluation of a Wind Turbulence Measurement System for Aircraft-Based Flux Measurements, *J. Atmos. Ocean Sci*, **23** (12), pp. 1696-1708.

Jasperon, W.H., Nastrom, G.D., Fritts, D.C., 1990, Further Study of Terrain Effects on the Mesoscale Spectrum of Atmospheric Motions, *J. Atmos. Sci.*, **47** (8), pp. 979-987.

Hazel, P., 1972, Numerical studies of the stability of inviscid stratified shear flows, *J. Fluid. Mech.*, **51**, pp.39-61

Joseph, B., Mahalov, A., Nicolaenko, B., Tse, K. L., 2004, Variability of Turbulence and Its Outer Scales in a Model Tropopause Jet, *J. Atmos. Sci.*, **61** (6), pp. 621–643

Kennedy, P.J., Shapiro, N.A., 1980, Further Encounters with Clear Air Turbulence in Research Aircraft, *J. Atmos. Sci.* **37**, pp. 986-993.

Kolmogorov, A. N., 1941: The local structure of turbulence in incompressible viscous fluid for very large Reynolds numbers. *Dokl. Akad. Nauk. SSSR*, **30**, 9-13.

Lindborg, E., 1999, Can the atmospheric kinetic energy spectrum be explained by two-dimensional turbulence? *J. Fluid Mech.* **388**, pp. 259-288.

Lindborg, E., Cho, J. Y. N., 2001, Horizontal Velocity Structure Functions in the Upper Troposphere and Lower Stratosphere 2. Theoretical Considerations, *J. Geophys. Res.* **106**, (10), pp. 10,233–10,241.

Lindborg, E., 2006, The energy cascade in a strongly stratified fluid. *J. Fluid Mech.*, **550**, pp. 207–242.

Marengo, A., Thouret V., Nedelec, P., Smith, H., Helten M., Kley, D., Karcher, F., Simon, P., Law, K., Pyle, J., Poschmann, G., Von Wrede, R., Hume, C. & Cook, T., 1998, Measurement of ozone and water vapor by airbus in-service aircraft: the MOZAIC airborne program, an overview. *J. Geophys. Res.* **103**, pp. 25631-25642.

Miles, 1961, On the stability of heterogeneous shear flows, *J. Fluid. Mech.*, **10**, pp.496-508.

Nastrom, G. D. and Jasperson, W.H., 1983, Flight Summaries and Temperature Climatology at Airliner Cruise Altitudes from Gasp (Global Atmospheric Sampling Program) Data, NASA CR-168106, Available from NTIS, N83240428.

Nastrom, G. D., Gage, K. S. 1985 A climatology of atmospheric wavenumber spectra of wind and temperature observed by commercial aircraft. *J. Atmos. Sci.* **42**, pp. 950-960.

Nastrom, G. D., Gage, K. S. & Jasperson, W. H., 1984 Kinetic energy spectrum of large- and mesoscale atmospheric processes. *Nature*, **310**, pp. 36-38.

Nichols-Page, G. A., Percival, D. B., Reinhalla, P.G., Riley, J.J., 2008, Should structure functions be used to estimate power laws in turbulence? A comparative study, *Physica D*, **237**, pp. 665–677.

Palmer, T. L., D. C. Fritts, Ø. Andreassen and I. Lie, 1994: Three-dimensional evolution of Kelvin-Helmholtz billows in stratified turbulence. *Geophys. Res. Letters*, **21**, 2287-2290.

Palmer, T. L., D. C. Fritts and Ø. Andreassen, 1996: Evolution and breakdown of Kelvin-Helmholtz billows in stratified compressible flows. Part II: Instability structure, evolution and energetic. *J. Atmos. Sci.*, **53**, 3192-3212.

Perkins, P.J., 1976, Global Measurements of Gaseous and Aerosol Trace Species in the Upper Troposphere and Lower Stratosphere, NASA-TMX-73544.

Riley and Lindborg, 2008, Stratified Turbulence: A Possible Interpretation of Some Geophysical Turbulence Measurements, *J. Atmos. Sci.*, **65**, pp. 2416-2424

Smyth, W. D. and J. M. Moum, 2000A: Length scales of turbulence in stably stratified mixing layers. *Phys. Fluids*, **12**, 1327–1342,

Smyth, W. D., J. M. Moum and D. R. Caldwell, 2001: The efficiency of mixing in turbulent patches: inferences from direct simulations and microstructure observations. *J. Phys. Oceanogr.*, **31**, 1969-1992.

Thorpe, S. A., 1969, Experiments on the instability of stratified shear flows: immiscible fluids. *J. of Fluid Mech.*, **39**, pp 25-48

Werne, J and Fritts, DC: 2000, Structure functions in stratified shear turbulence. 10th *DoD HPC User Group Conference*, Albuquerque, NM.

Werne, J. and D. C. Fritts, 1999: Stratified shear turbulence: evolution and statistics. *Geophys. Res. Letters*, **26**, 439-442.

Werne, J, T. Lund, B.A. Pettersson-Reif, P. Sullivan, and D.C. Fritts, 2005, CAP Phase II Simulations for the Air Force HEL-JTO Project: Atmospheric Turbulence Simulations on NAVO's 3000-Processor IBM P4+ and ARL's 2000-Processor Intel Xeon EM64T Cluster, 15th *DoD HPC User Group Conference*, Nashville.

Werne, J., Lund, T., Fritts, D., Pettersson-Reif, B. A., Andreasson, O., Wroblewski, D., Berliner., M., 2008, "Clear Air Turbulence (CAT) Simulation and Observation: Implications for Parameterization, Workshop on Petascale Computing: Its Impact on Geophysical Modeling and Simulation, Boulder, 5/2008.

Whiteway, J.A., G. P. Klaassen, N. G. Bradshaw, and J. Hacker, 2003A: Transition to Turbulence in Shear Above the Tropopause. *Geophys. Res. Lett.*, **31**.

Whiteway, J. A., E. G. Pavelin, R. Busen, J. Hacker, and S. Vosper, 2003B, Airborne measurements of gravity wave breaking at the tropopause, *Geophys. Res. Lett.*, **30**(20), 2070, doi:10.1029/2003GL018207.

Wroblewski, D. E., Cote, O.R., Hacker, J.M., Dobosy, R., J., 2007, Cliff-Ramp Patterns and Kelvin-Helmholtz Billows in Stably Stratified Shear Flow in the Upper Troposphere: Analysis of Aircraft Measurements, *J. Atmos. Sci.*, 64 (7), pp. 2521-2539.

Wroblewski, D., Cote, O., Hacker, J., Dobosy, R., “Velocity and Temperature Structure Functions in the Upper Troposphere and Lower Stratosphere from High Resolution Aircraft Measurements,” 2009, submitted to *J. of Atmos. Sciences.*

Table 1 Summary of flights

Dates	Loc.	# levels	Alt, km	f_s , Hz	D , km
1998: 8/25-9/03	SA	25	6.8-14.2	55.6	1,900
1999: 2/03-2/21	JA	19	5.8-12.4	58.8	2,026
1999: 8/6	SA	7	9.0-12.2	58.8	710
2000: 5/10-6/6	WA	20	8.1-13.8	55.6	2,112
2001: 8/17-8/24	SA	15	8.5-10.8	55.6	1,335
2002: 8/28-9/16	SA	37	7.1-14.0	50	4,101
2002: 11/22	DA	5	9.6-14.4	25	442
2006: 8/6	SA	1	8.5	10	50

SA- South Australia; JA- Japan;
 WA- Wales; DA- Darwin,
 Australia
 f_s - sampling frequency

Table 2: Results of quantitative comparisons of aircraft flights with DNS.

Date	Vertical Location	Time	Ri	Comments
990213	Off-cen	La	Ind	Bu, rCR, CB, VC
990806	Center	Mid	Hi	CR, SC, VC
000606	Center	La	Hi	CR
020830 _A	Off-cen	La	Ind	Bu, CR, VC
020830 _B	Off-cen	La	Ind	Bu, CR CB
020831	Center	La	Hi	CR
020905	Center	La	Med	CR, CB
021122	Center	Mid	Med	CR, SC
060809	Center	La	Hi	CR, CB
060819	Off-cen	La	Ind	Bu, rCR

Bu=Buttes
 CR=Cliff-ramps
 rCR=Cliff-ramps with rounded edges
 SC=Stair-cliffs
 VC= Velocity cliffs
 CB=Cliff Breakdown

Table 3: Results of quantitative comparisons of aircraft flights with DNS. h = initial layer height; H = final layer height; U_0 =velocity scale; S_0 = initial shear; Δt =cliff ramp duration

Date	990213	990806	000606	020905	020830 _A	020830 _B	020831	021122	060809	060819
$\Delta\theta/\beta\lambda$	0.062	0.139	0.0871	0.0798	0.089	0.195	0.231	0.199	0.11	0.0383
Ri_1	0.227	0.183	0.216	0.220	0.204	0.141	0.128	0.138	0.205	0.231
Ri_2	0.229	0.198	0.220	0.223	0.214	0.161	0.150	0.159	0.210	0.235
h_1, m	86	750	141	132	165	237	56	132	79	220
h_2, m	86	768	142	132	168	246	59	137	79	222
H_1, m	135	2017	261	233	359	874	224	494	168	326
H_2, m	131	1783	250	224	323	790	204	448	160	304
U_{01}, ms^{-1}	4.3	18.3	5.2	4.7	5.0	10.3	1.5	5.1	3.4	7.2
U_{02}, ms^{-1}	4.2	17.6	5.2	4.7	4.9	9.6	1.3	4.8	3.4	7.2
S_{01}, s^{-1}	0.055	0.025	0.040	0.039	0.032	0.042	0.024	0.037	0.046	0.036
S_{02}, s^{-1}	0.054	0.024	0.040	0.038	0.031	0.039	0.022	0.034	0.046	0.036
$\Delta t_1, s$	301	380	367	392	397	89	84	92	279	470
$\Delta t_2, s$	309	488	383	407	454	164	218	177	299	493

Table 4: Structure parameters and isotropy ratios for composite structure functions

$\text{Log}_{10}C_L^2$ range	ALL	>-2.52	-3.24 to -2.52	< -3.24
n_L	0.66	0.67	0.71	0.46
n_N	0.70	0.71	0.73	0.52
n_W	0.76	0.82	0.6	0.46
$C_L^2 (m^{4/3} s^{-2})$	$6.22 \cdot 10^{-3}$	$1.85 \cdot 10^{-2}$	$1.44 \cdot 10^{-3}$	$3.31 \cdot 10^{-4}$
$\epsilon, (m^2 s^{-3})$	$1.73 \cdot 10^{-4}$	$8.92 \cdot 10^{-4}$	$1.93 \cdot 10^{-5}$	$2.13 \cdot 10^{-6}$
C_N^2 / C_L^2	0.88	0.87	1.00	0.78
C_W^2 / C_L^2	0.60	0.61	0.64	0.60
$\text{Log}_{10}C_T^2$ range	ALL	< -3.92	-4.67 to -3.92	>-4.67
$C_T^2 (K^2 m^{-2/3})$	$3.25 \cdot 10^{-4}$	$9.26 \cdot 10^{-4}$	$6.54 \cdot 10^{-5}$	$1.10 \cdot 10^{-5}$
n_T	0.70	0.78	0.67	0.67

Table 5: Comparisons of aircraft data for five cliff-ramp cases with radiosonde data analyzed using RiNLAW. EDR is Eddy Dissipation Rate, $EDR=\epsilon^{1/3}$.

Date	Aircraft Data		Radiosonde	
	Layer Alt (km)	EDR	Layer Alt (km)	Ri
990213	9.1	0.10	10.3-10.7	0.22
990806	9.7	0.57	9.6-10.0	0.25
000606	11.4	0.23	12.0-12.1	0.17
020830	14.1	0.17	15.8-16.3	0.38
020831	6.1	0.10	5.1-5.6	0.27
020905	8.3	0.31	7.2-7.4	0.08
060809	8.5	0.12	8.3-8.6	0.20
060819	9.7	0.13	9.8-10.1	0.36

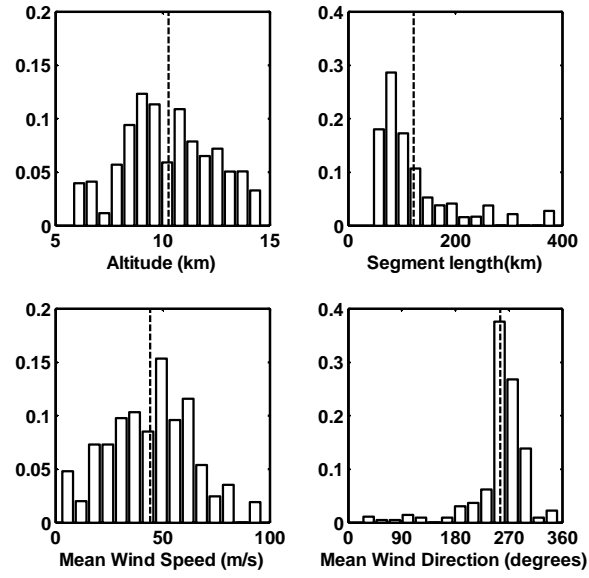


Figure 1: Histograms showing distributions of flight parameters. Dashed lines mark mean values.

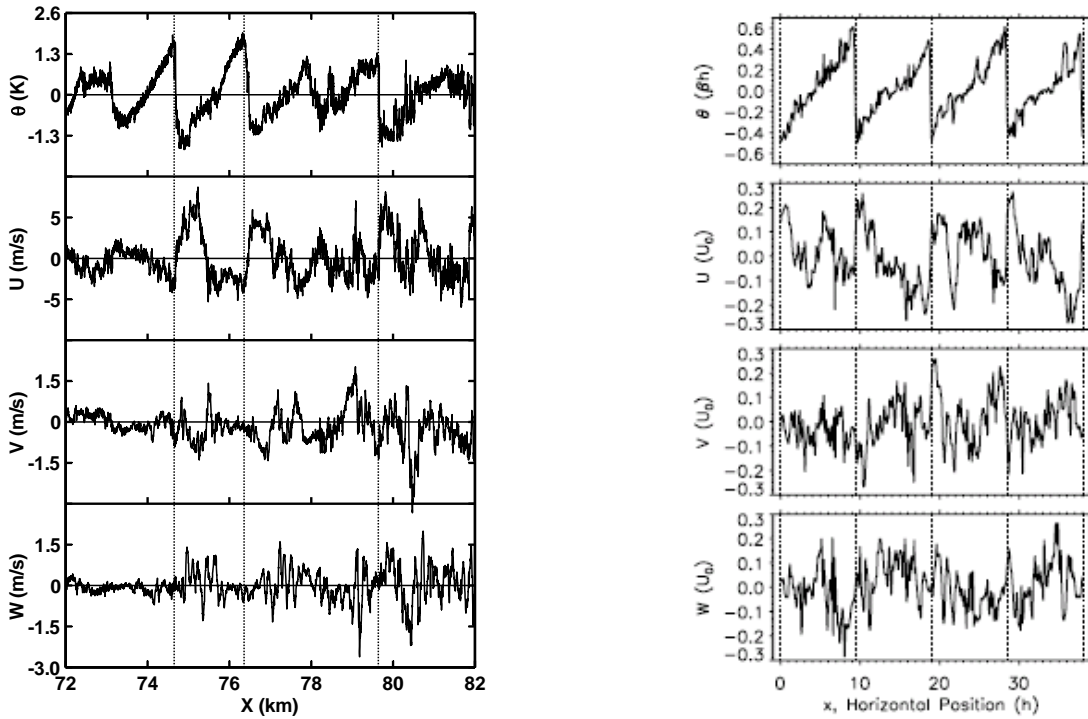


Figure 2: Potential temperature and velocity: (a) aircraft data for 000606, 11.4 km. (b) DNS for $Ri=0.2$, $z/H=0$, $tU_0/h=77$.

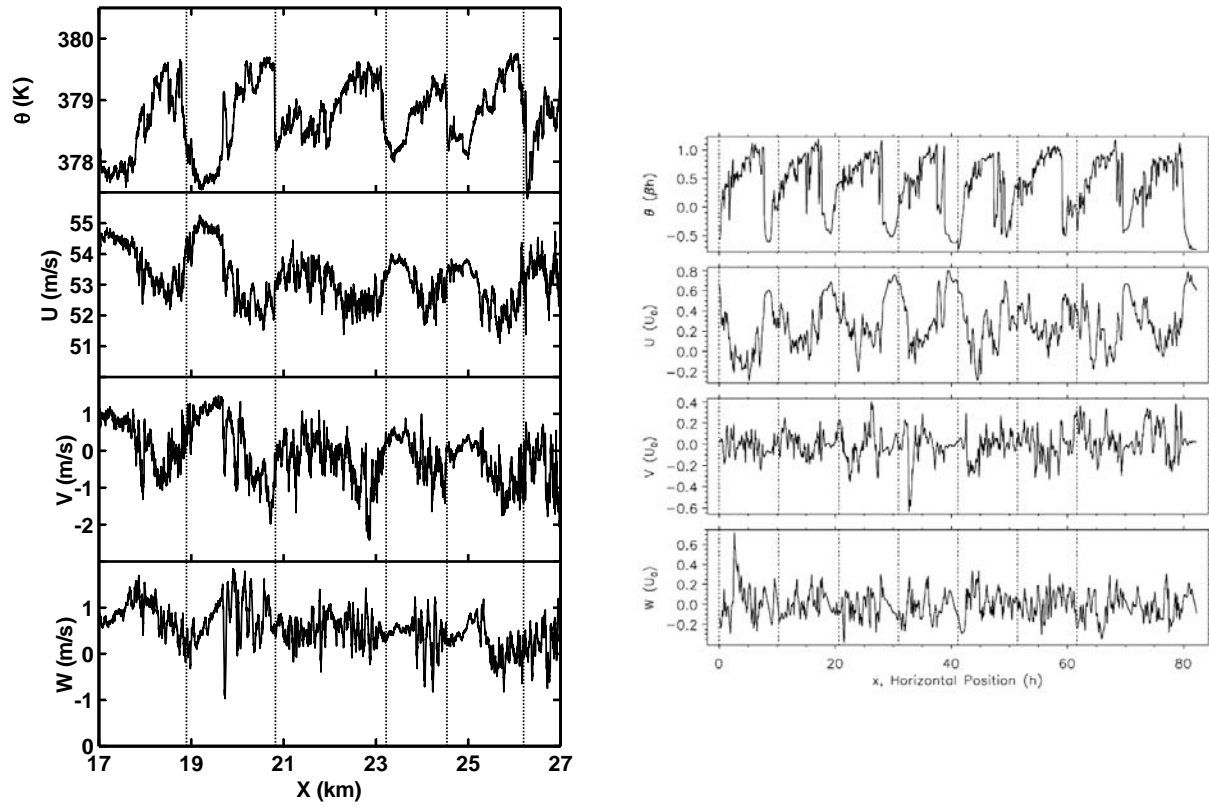


Figure 3: Potential temperature and velocity: (a) aircraft data for 020830, 14.3 km. (b) DNS for $Ri=0.15$, $z/H=0.125$, $tU_0/h=76.1$.

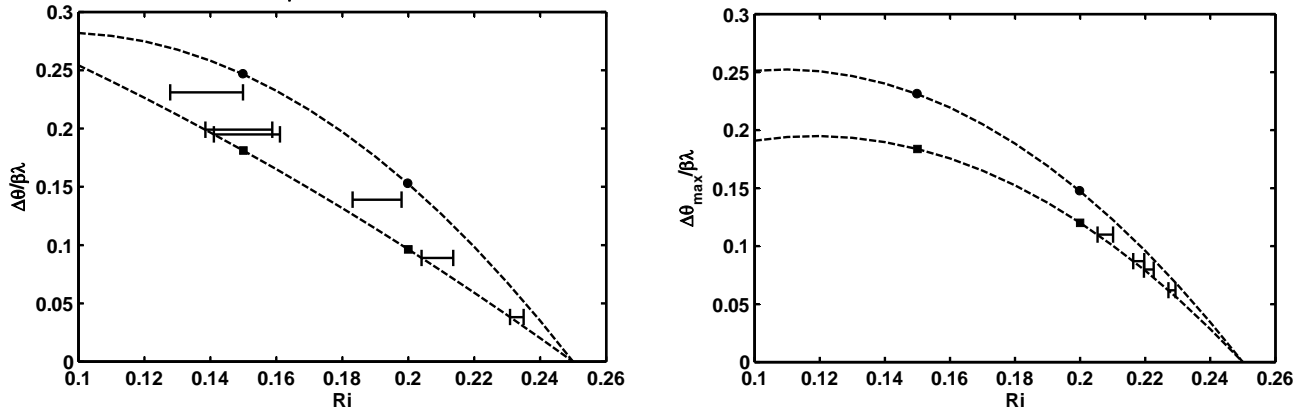


Figure 4: Temperature change across cliff in cliff-ramps ($\Delta\theta$) normalized on vertical temperature gradient, β , and cliff-ramp wavelength, λ , as a function of Richardson number for $z/H=0$ (left) and $z/H=0.125$ (right). Closed symbols are values from DNS: circles are for the beginning of cliff-ramp phase of billow development and squares are for the end. Dashed lines are curves fit to data. Horizontal lines are values for the aircraft flights, indicated ranges of estimated Ri .

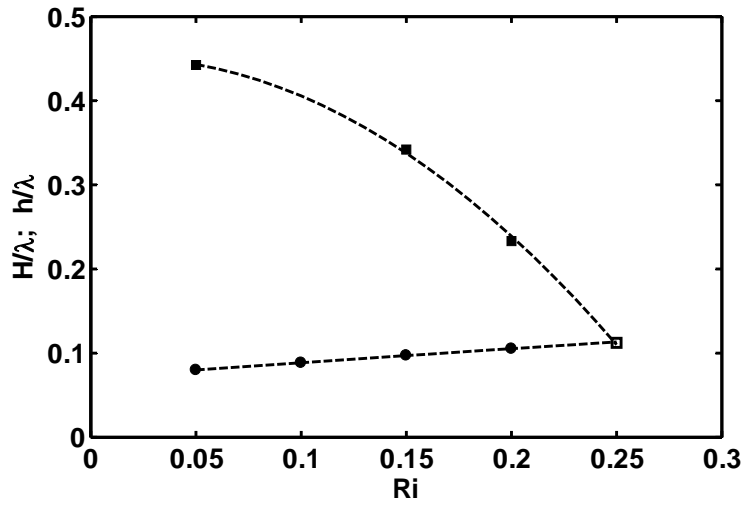


Figure 5: Final billow height (H), square symbols, and initial billow height (h), circle symbols, as a function of initial Ri , normalized on billow wavelength (λ).

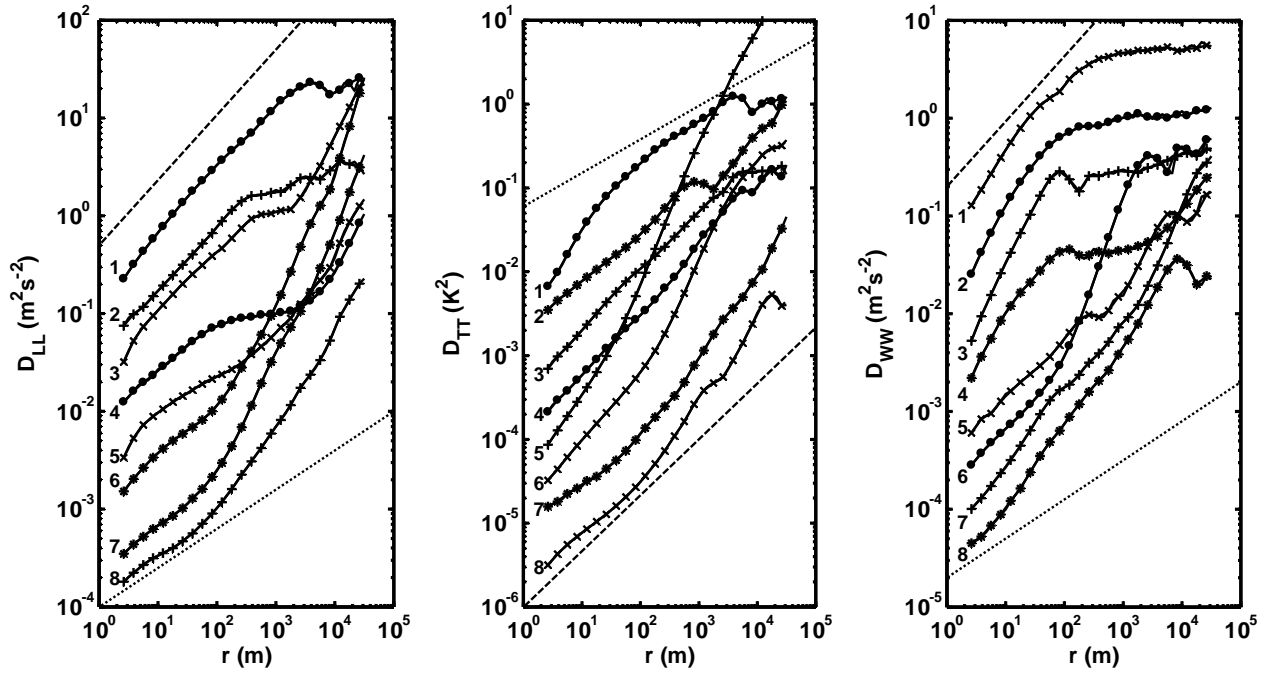


Figure 6: Structure functions as a function of separation distance for selected individual flight segments. Dashed line shows $r^{2/3}$; dotted line shows $r^{2/5}$.

D_{LL} (left plot) 1--6 Aug, 1999, 9.7 km; 2--23 Aug, 2001, 9.3 km; 3--6 June., 2000, 11.4 km (Wales); 4--17 Aug., 2001, 10.6 km; 5--10 May, 2000, 12.3 km (Wales); 6--6 June, 2000, 9.9 km (Wales); 7--26 Aug, 1998, 6.6 km; 8--20 Feb., 1999, 10.9 km (Japan).

D_{TT} (middle plot): 1--6 Aug, 1999, 9.7 km; 2--6 June, 2000, 11.4 km (Wales); 3--23 Aug, 2001, 9.3 km; 4--26 Aug., 1999, 12.5 km; 5--11 May, 2000, 12.3 km (Wales); 6--18 May, 2000, 13.8 km (Wales); 7--24 Aug., 2001, 8.7 km; 8--6 Aug, 1999, 12.2 km.

D_{WW} (right plot): 1--6 Aug, 1999, 9.7 km; 2--23 Aug, 2001, 9.3 km; 3--6 June, 2000, 11.4 km (Wales); 4--17 Aug., 2001, 10.6 km; 5--3 Sept, 1998, 6.8 km; 6--21 Feb., 1999 6.8 km (Japan); 7--20 Feb, 1999, 9.3 km (Japan); 8--6 Aug, 1999, 12.2 km.

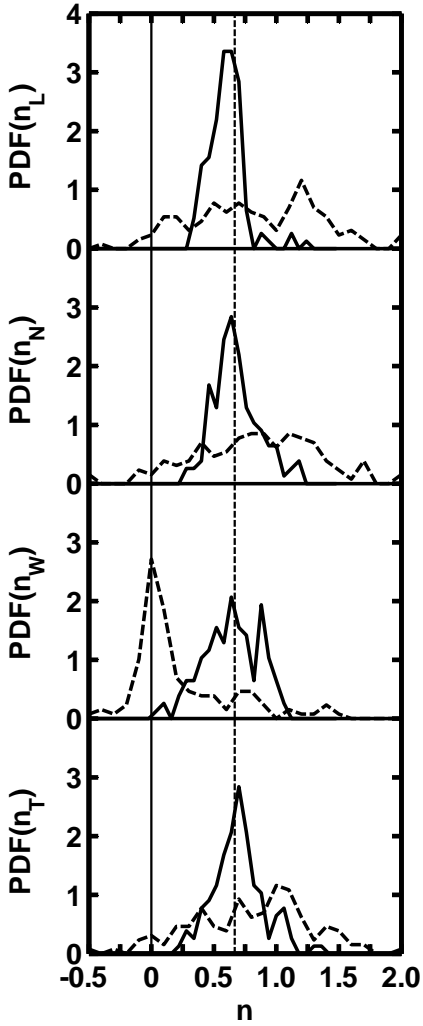


Figure 7: Distributions of exponents, n_x , for velocity and temperature structure function; $D_{XX} \propto r^{n_x}$, where $X=L,T,W$, or N . Vertical dashed line is $2/3$.

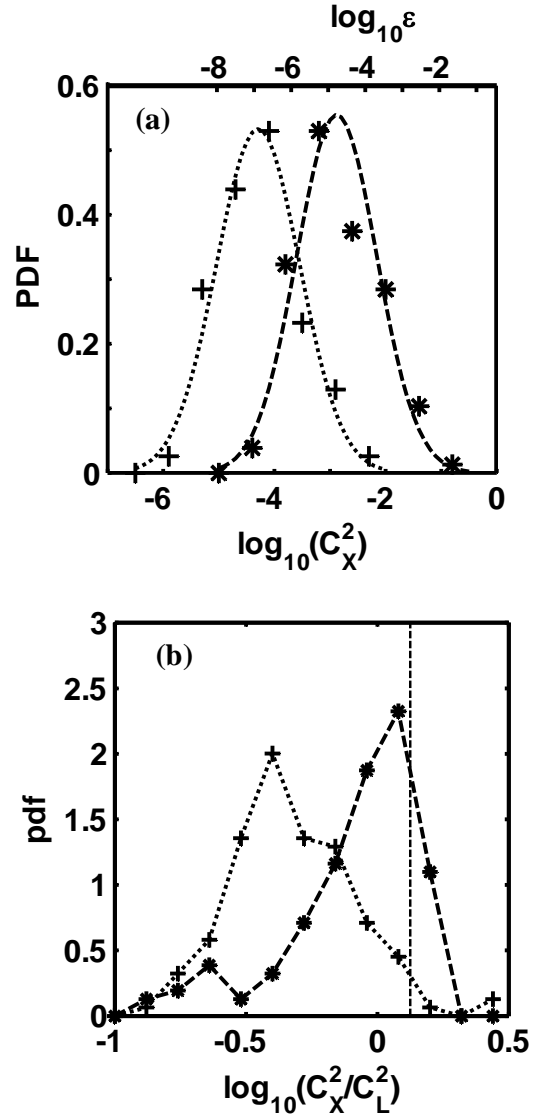


Figure 8: (a) Distributions of longitudinal velocity and temperature structure parameters in 3D scale range; Asterisks, C_L^2 ; crosses, C_T^2 ; dashed line, lognormal fit for C_L^2 ; dotted line, lognormal fit for C_T^2 . (b) Distributions of ratios of structure parameters for normal and vertical velocity to structure parameters for longitudinal velocity in 3D scale range; Asterisks, C_N^2/C_L^2 ; crosses, C_W^2/C_L^2 ; vertical line, isotropic value of $4/3$.

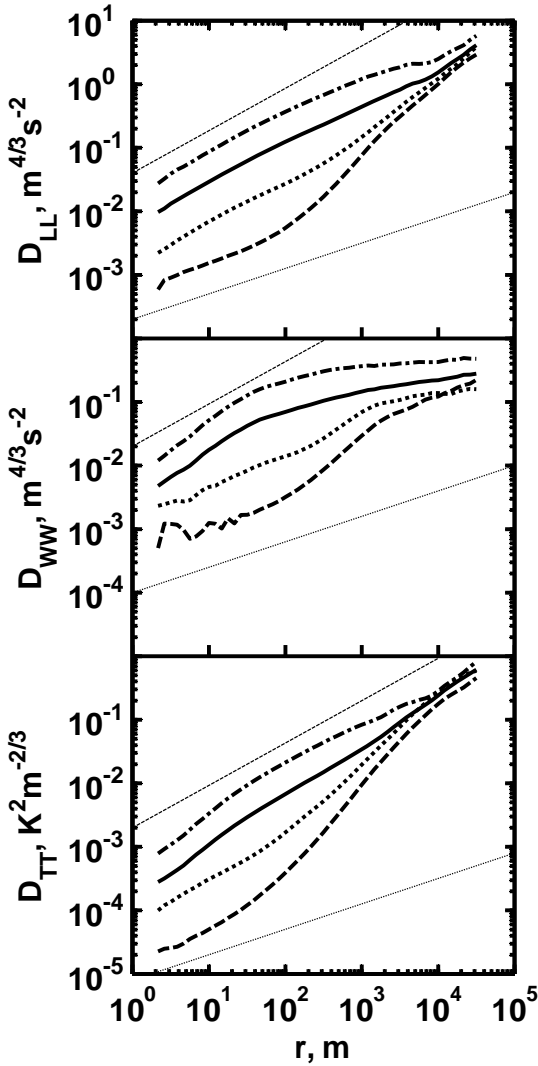


Figure 9: Composite structure functions as a function of separation distance for sub-ensembles of levels. Solid line, all levels; dashed line, weak turbulence- all levels with $\log(C_L^2)$ or $\log(C_T^2)$ less than $\frac{1}{2}\sigma$ below mean; dotted line, moderate turbulence-- all levels with $\log(C_L^2)$ or $\log(C_T^2)$ within $\frac{1}{2}\sigma$ of mean; dot-dash line, strong turbulence- - all levels with $\log(C_L^2)$ or $\log(C_T^2)$ greater than $\frac{1}{2}\sigma$ above mean. Thin dashed lines show $r^{2/3}$. Thin dotted line shows $r^{2/5}$.

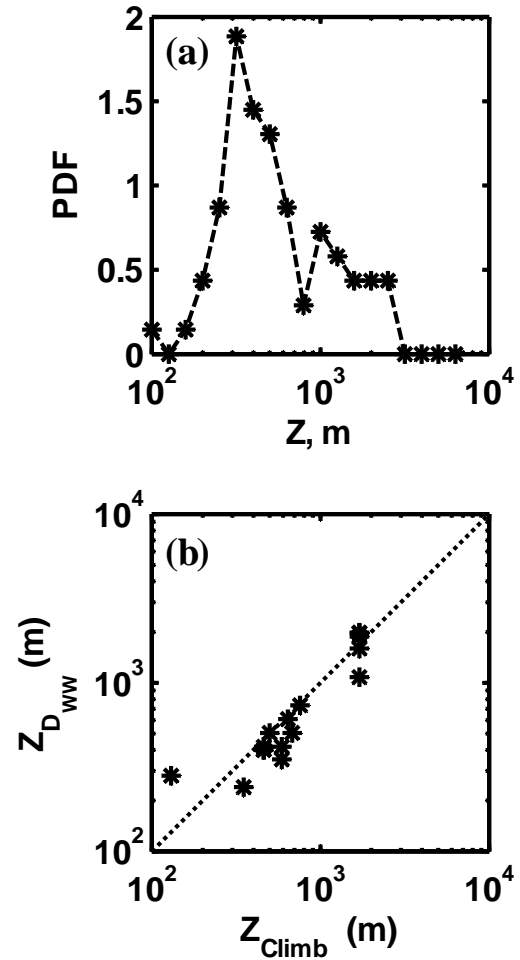


Figure 10: (a) Log distribution of layer height for 69 layer-height cases. (b) Layer heights as a function of layer heights estimated from climb data for selected levels.

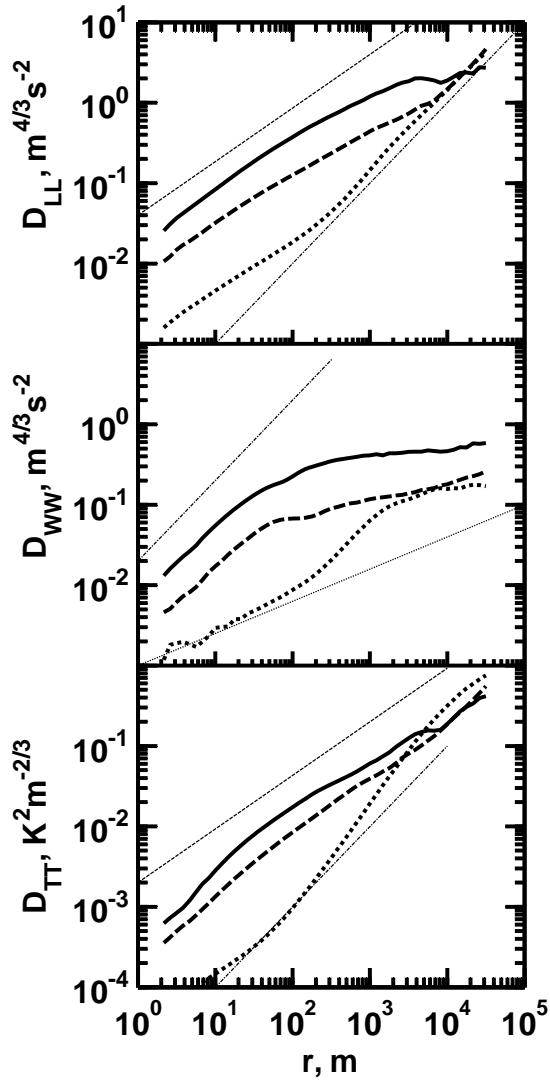


Figure 11: Composite structure functions as a function of separation distance for sub-ensembles of levels. Solid line, layer-height cases with $Z > 700$ m; dashed line, layer-height cases with $Z < 700$ m; dotted line, all levels excluding layer-height cases. Thin dashed lines show $r^{2/3}$. Thin dotted lines show $r^{2/5}$. Thin dash-dot lines show r^1 .

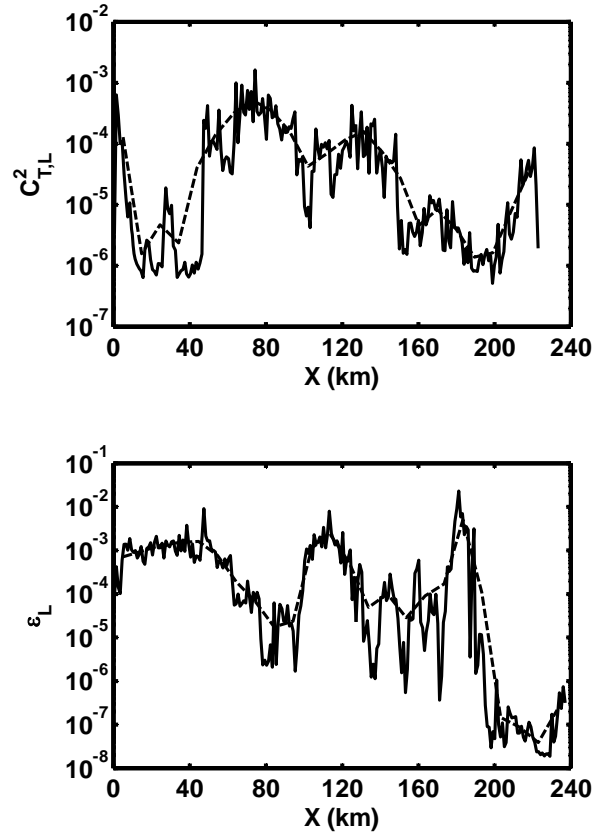


Figure 12: Short time structure functions: $C_{T,L}^2$ (top) dissipation (bottom). Solid lines, 1 km averaging window; dashed line, 10 km averaging window.

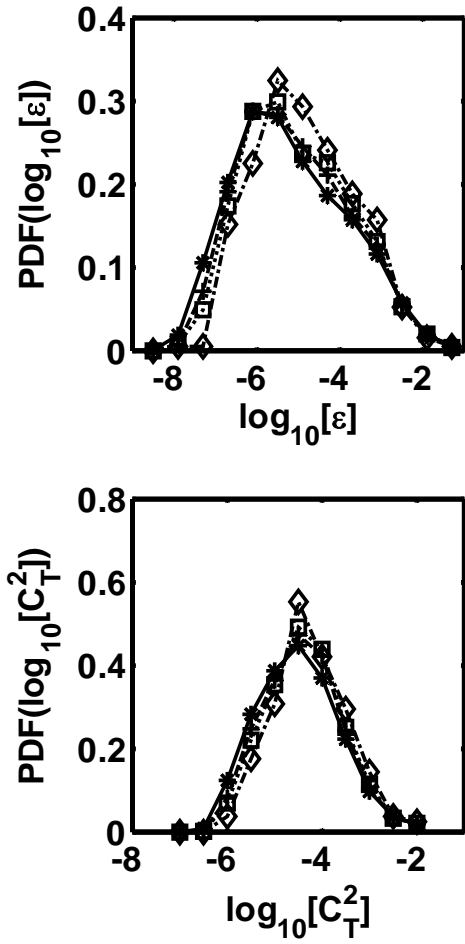


Figure 13: Distributions of short time dissipation (top) and C_T^2 (bottom) for all 129 CAT layers for different averaging window sizes: 1 km window * symbols; 5 km window + symbols; 10 km window □ symbol; 45 km window ◇ symbols.

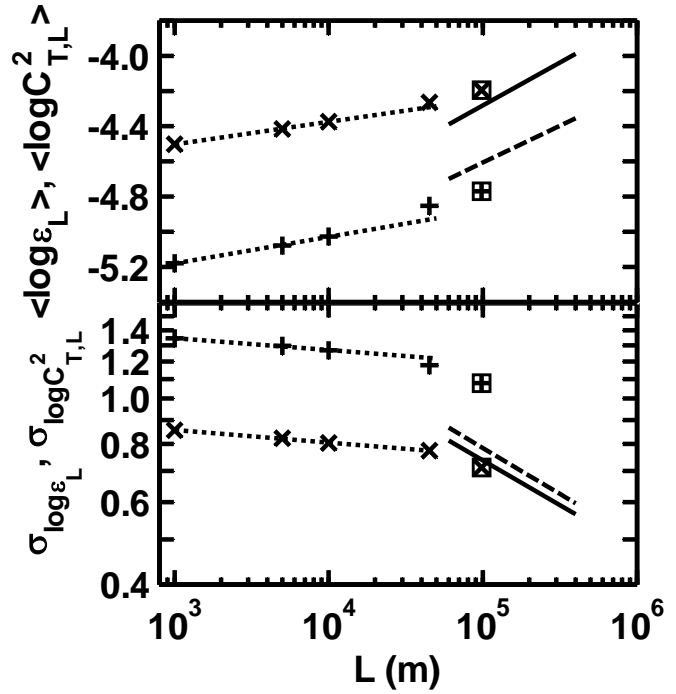


Figure 14: Mean and standard deviation for lognormal fits to ε and C_T^2 distributions as a function of averaging length-- 30 m separation length for ε and 90 m separation distance for C_T^2 . x symbols C_T^2 ; + symbols ε ; dotted lines, curve fit using smallest three averaging lengths (1 km, 5 km, 10 km); dashed lines and solid lines, curve fits from FS05 for ε and C_T^2 .

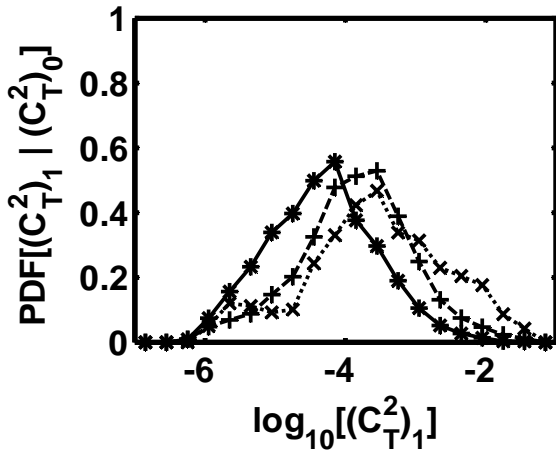
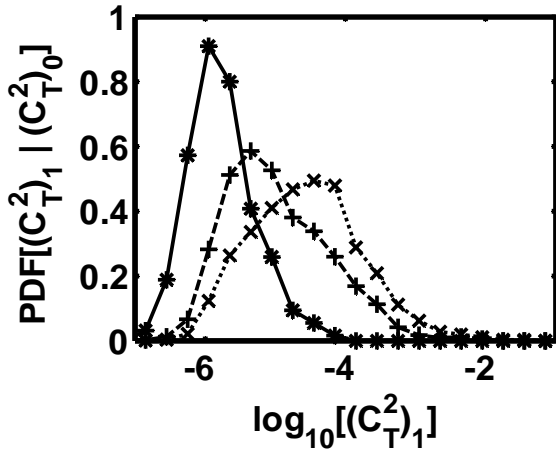


Figure 15: Conditional probability density functions for short time C_T^2 : $P[(C_T^2)_1 | (C_T^2)_0]$. Top plot: $(C_T^2)_0 = -6.55 \pm 0.15$ (* symbol), $(C_T^2)_0 = -5.65 \pm 0.15$ (+ symbol), $(C_T^2)_0 = -4.75 \pm 0.15$ (x symbol). Bottom Plot: $(C_T^2)_0 = -3.85 \pm 0.15$ (* symbol), $(C_T^2)_0 = -2.95 \pm 0.15$ (+ symbol), and $(C_T^2)_0 = -2.05 \pm 0.15$ (x symbol).

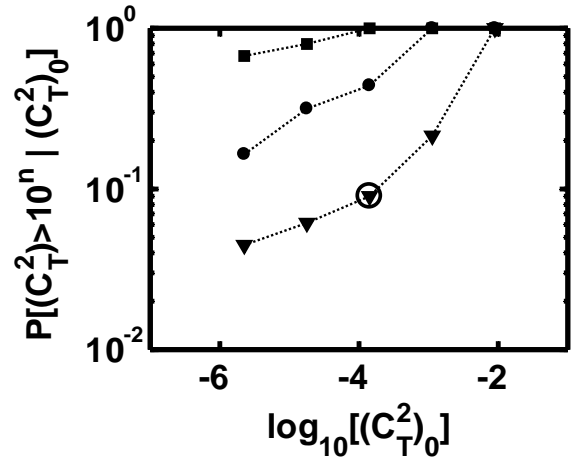
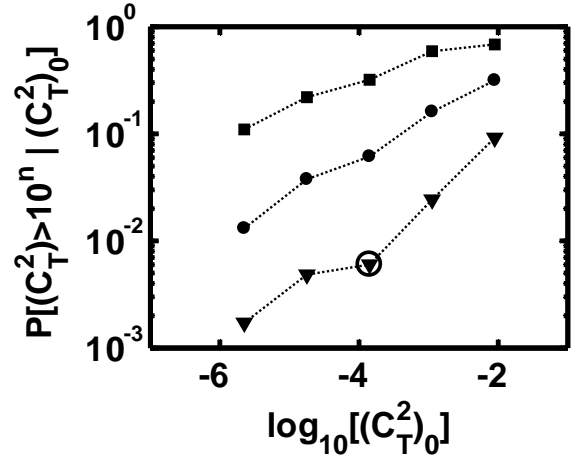


Figure 16: Conditional probability density functions for short time C_T^2 : $P[(C_T^2) > 10^n | (C_T^2)_0]$. With thresholds of $n = -4$ (squares), -3 (circles), and -2 (triangles). Top: probability that a random realization will exceed the threshold. Bottom: probability that at least one realization will exceed threshold.

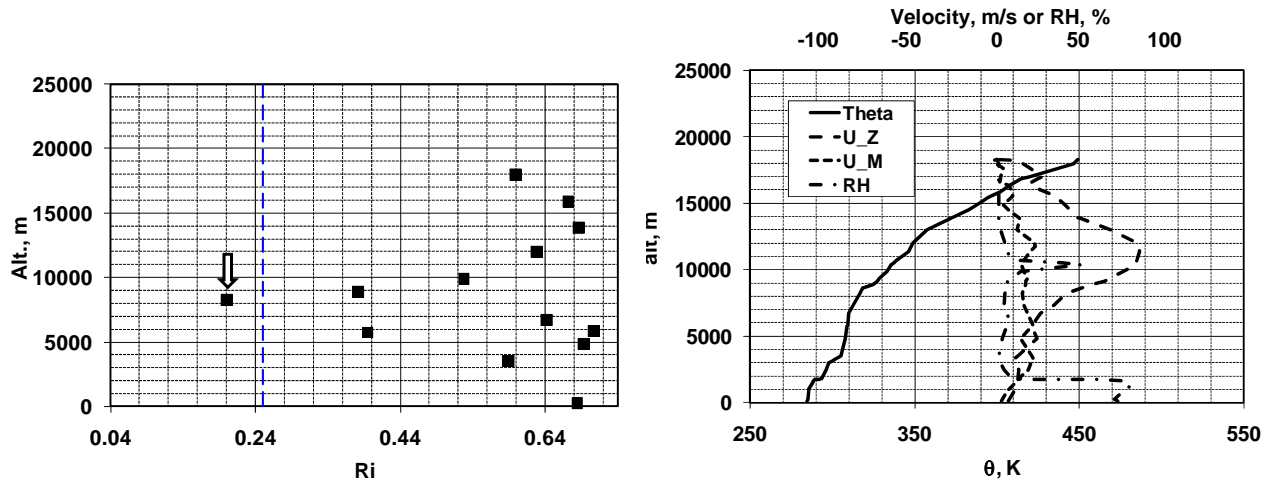


Figure 17: Layer Richardson number and wind and temperature profiles for Adelaide, Australia 9 Aug., 2006. Note single layer with Ri below 0.25 near 8.3 km (arrow).

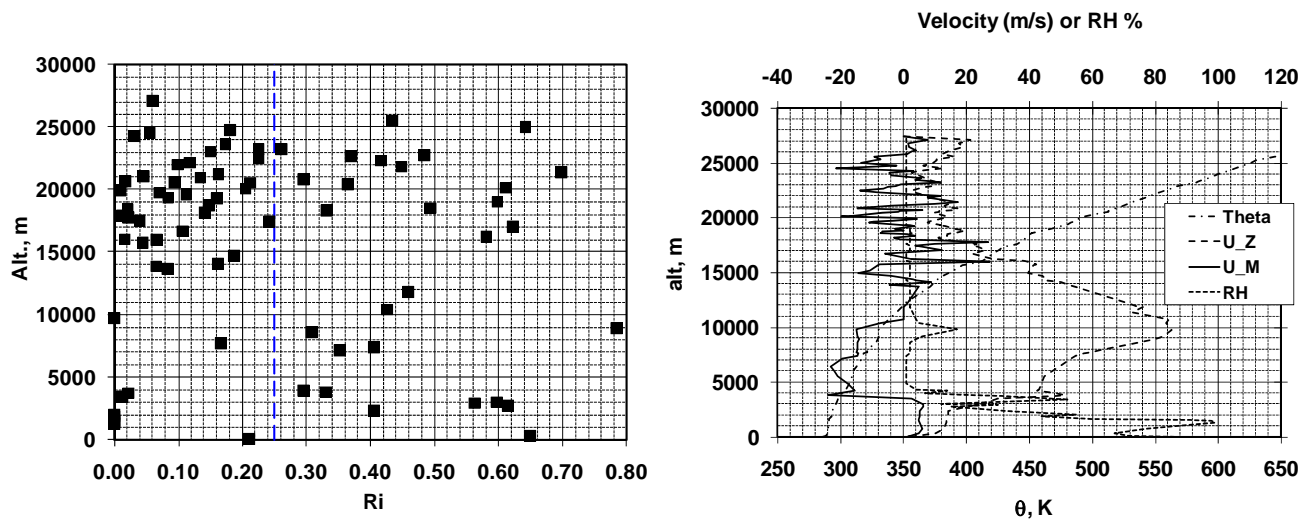


Figure 18: Layer Richardson number and wind and temperature profiles; Perth, Australia 15 July, 2008.

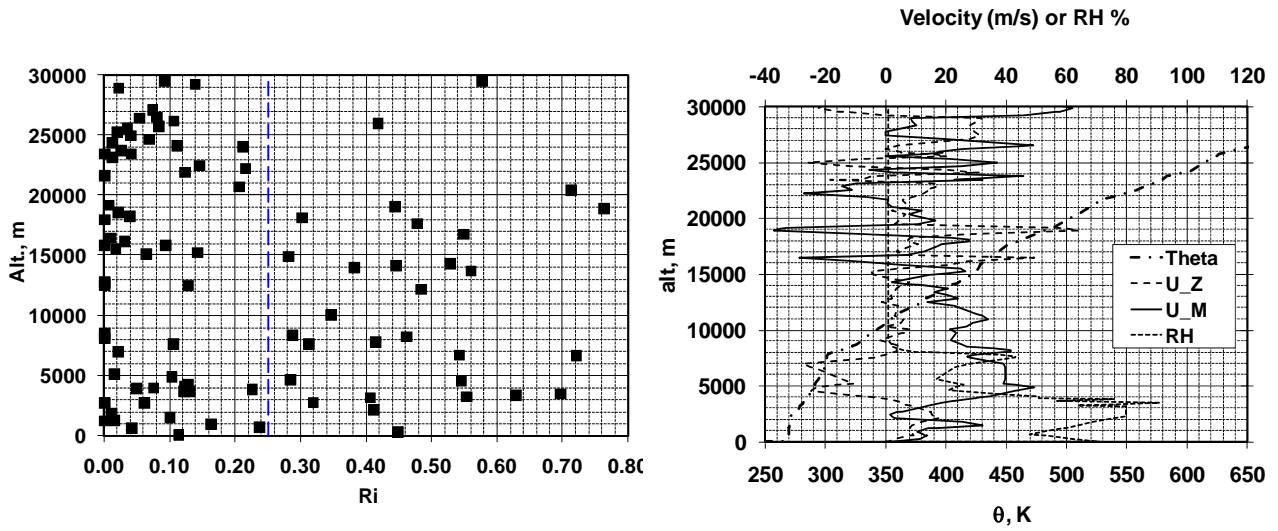


Figure 19: Layer Richardson number and wind and temperature profiles; Goose bay, Canada 24 Nov., 2008.

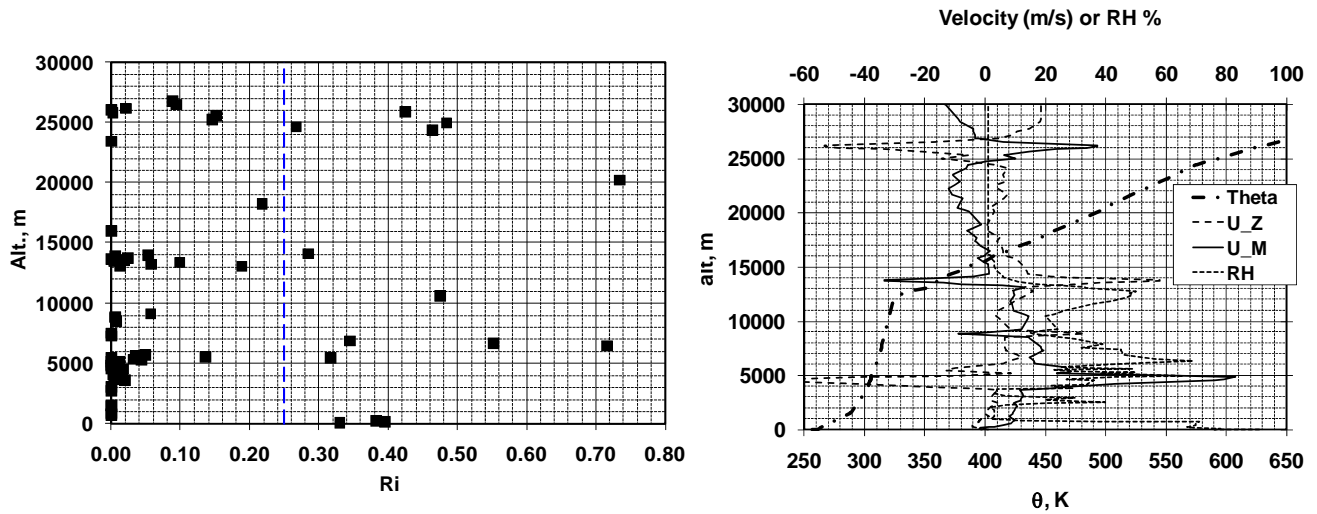


Figure 20: Layer Richardson number and wind and temperature profiles; Goose bay, Canada 27 Nov., 2008.

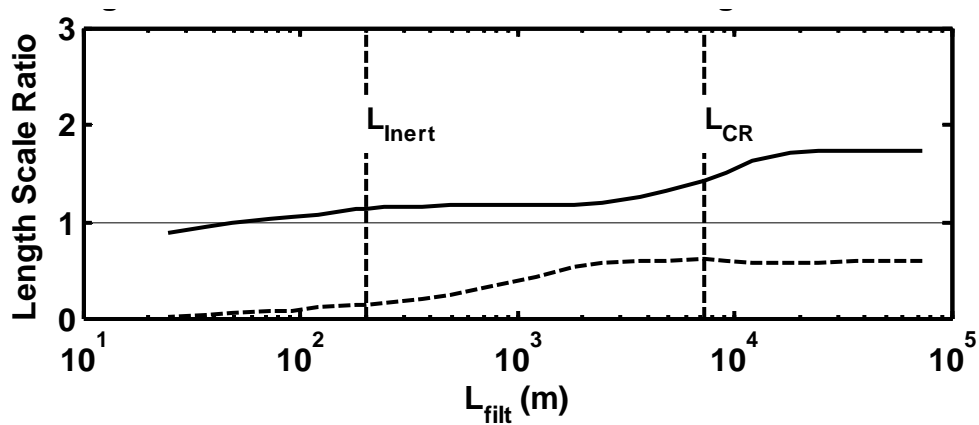


Figure 21: Length scale ratios as a function of filtering length scale. Solid line, L_E/L_B ; dashed line, L_{DW}/L_E .

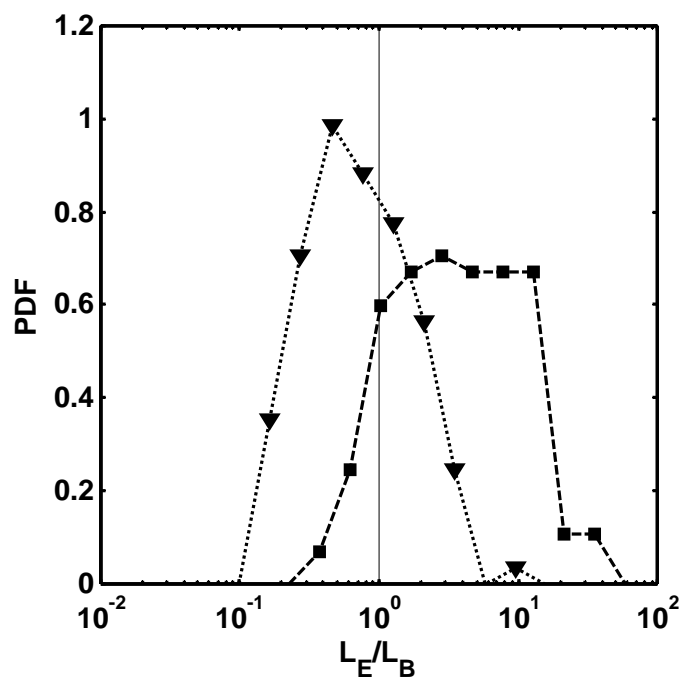


Figure 22: Distribution of the L_E/L_B for all 129 CAT levels. Squares/dashed line, unfiltered; triangles/dotted line, filtered at inertial sub-range scale.